Research Article | Vol. 29, No. 24 / 22 Nov 2021 / Optics Express 40051
Optics EXPRESS

STED microscopy reveals in-situ photoluminescence properties of single nanostructures in densely perovskite thin films

QINGYA WANG,[1,7] QILIN QIN,[2,7] YUHAN CHEN,[1,7] TIESHAN YANG,[3,7] QINFENG XU,[1,4] HAIFENG MU,[1] JING HAN,[1] KUNJIAN CAO,[1] MENGMENG JIAO,[1] MINGLIANG LIU,[1] SHUFANG ZHANG,[1,5] AND CHUANLU YANG[1,6]

[1]*Department of Physics and Optoelectronic Engineering, Ludong University, Yantai 264025, China*
[2]*National Laboratory of Solid State Microstructures, School of Physics, and Collaborative Innovation Center of Advanced Microstructures, Nanjing University, Nanjing 210093, China*
[3]*School of Mathematical and Physical Sciences, University of Technology Sydney, Ultimo, New South Wales 2007, Australia*
[4]*xuqf5678@163.com*
[5]*zhangshufang98@126.com*
[6]*yangchuanlu@126.com*
[7]*Co-first Authors*

Abstract: All-inorganic perovskite nanomaterials have attracted much attention recently due to their prominent optical performance and potential application for optoelectronic devices. The carriers dynamics of all-inorganic perovskites has been the research focus because the understanding of carriers dynamics process is of critical importance for improving the fluorescence conversion efficiency. While photophysical properties of excited carrier are usually measured at the macroscopic scale, it is necessary to probe the in-situ dynamics process at the nanometer scale and gain deep insights into the photophysical mechanisms and their localized dependence on the thin-film nanostructures. Stimulated emission depletion (STED) nanoscopy with super-resolution beyond the diffraction limit can directly provide explicit information at a single particle level or nanometer scale. Through this unique technique, we firstly study the in-situ dynamics process of single $CsPbBr_3$ nanocrystals(NCs) and nanostructures embedded inside high-dense samples. Our findings reveal the different physical mechanisms of PL blinking and antibunching for single $CsPbBr_3$ NCs and nanostructures that correlate with thin-film nanostructural features (e.g. defects, grain boundaries and carrier mobility). The insights gained into such nanostructure-localized physical mechanisms are critically important for further improving the material quality and its corresponding device performance.

1. Introduction

Since the first report of the organic−inorganic hybrid halide perovskites in solar cells [1], the power conversion efficiency of perovskite solar cells [2–5] has been improved significantly over the past few years. Compared to the vulnerable organic−inorganic hybrid halide perovskites (e.g. $MAPbI_3$), $CsPbX_3$ (X = Cl, Br, I) is a promising inorganic perovskite material with strong stability against oxygen, moisture and heat. Therefore, inorganic perovskite materials (quantum dots [6–10] and thin films [11–16]) have attracted extensive attention recently. Tremendous efforts have been made to gain deep insight into fundamental optoelectronic properties and improve their photovoltaic performance. The device performance is strongly influenced by the perovskite microstructure [17–19] and film morphology [20,21]. Grain-to-grain variability in microstructure with grain boundaries [22,23] and defect concentrations [24] can be found within the same

#442345 https://doi.org/10.1364/OE.442345
Journal © 2021 Received 9 Sep 2021; revised 18 Oct 2021; accepted 26 Oct 2021; published 16 Nov 2021

Optics EXPRESS

$CsPbX_3$(X = Cl, Br, I) perovskite thin film. As a result, the local properties of $CsPbX_3$(X = Cl, Br, I) perovskite thin films are variable at the nanometer scale or individual particle level, which in turn influence the fundamental optical performance. Therefore, optoelectronic properties of perovskite devices, including charge carrier transport and recombination can be largely influenced by the interaction dynamics of nanostructures. Although intensive investigations have been carried out at the macroscopic scale, the microscopic in-situ photophysical properties of the excited carriers are still far from fully being understood at a nanostructure level or nanometer scale. Therefore, it is necessary to probe in-situ dynamics processes at the nanometer scale to gain deep insights into the fundamental physical mechanisms and their localized dependence on the perovskite $CsPbX_3$ thin-film nanostructures.

In order to obtain a detailed understanding the interaction of nanostructured materials and its local photophysical properties of perovskite thin films at the nanometer scale, several scanning probe methods, such as scanning electron microscopy (SEM) [25–28], transmission electron microscopy (TEM) [29,30] and atomic force microscopy(AFM) [31] have been used. However, for the aforementioned techniques, they all need highvacuum conditions. In addition, some of them are invasive with poor contrast. As a result, the sample preparation is complicated and timeconsuming which makes them unreliable to investigate in-situ dynamic processes. In contrast, stimulated emission depletion (STED) nanoscopy [32–36] providing explicit information which cannot be extracted from an ensemble measurement, is an effective method with super-resolution beyond the diffraction limit and is increasingly used to investigate the morphology and in-situ dynamic behavior at the nanometer scale. Therefore, an in-depth study of perovskites in situ dynamics process at a nanostructure level or nanometer scale is significant to further improve the material quality and its corresponding device performance.

In this work, we used STED nanoscopy to systematically investigate in-situ dynamics process of single $CsPbBr_3$ nanocrystals(NCs) and single nanostructure embedded inside high-dense samples. Compared with confocal system, the in-situ fluorescence behavior and carrier dynamics of single $CsPbBr_3$ NCs and single nanostructure embedded inside high-dense samples can be resolved at the single particle level or nanometer scale. We investigated the fluorescence characteristics of single nanostructure and revealed that the single-photon emission signature and fluorescence blinking in high-dense samples due to different physical origins. These measurements are likely to provide key insights into the local nanostructured effects on the optical performance and are essential for guiding the nanostructured tailoring of perovskite thin films for higher conversion efficiency in the future.

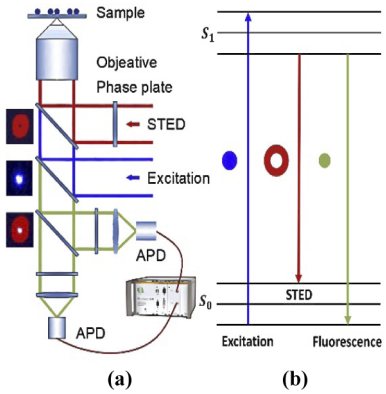

Fig. 1. (a) Schematic illustration of the setup for STED nanoscopy and (b) the mechanism of spontaneous fluorescence emission and stimulated emission of $CsPbBr_3$ QDs.

Optics EXPRESS

2. Experimental setup

Figure 1(a) provides a schematic illustration of the STED nanoscopy system. The STED nanoscopy system consists of excitation, depletion and detection. In the experiment system, the excitation beam is 405 nm with 5-20 MHz tunable repetition frequency pulse laser and the depletion beam is a 568 nm continuous laser. When the STED depletion beam is coaxial with the excitation beam, the diffraction-limited excitation focus is overlaid by the STED beam forming a doughnut-shaped point-spread function(PSF). The STED beam depletes the fluorescent excitation state everywhere within the overlapping region by means of stimulated emissions, except for the center hole of the doughnut shape. As a result, only the fluorescence emitters in the hole are excited and form the effective fluorescence point beyond the diffraction limit.

Very recently, the synthesis of $CsPbX_3$ (X = Cl, Br, I) all-inorganic perovskite nanocrystals have been developed [37–39]. The $CsPbX_3$ nanocrystals combine the advantages of high photoluminescence quantum yield (PLQY>90%) and very broad emission spectrum at around λ~520 nm (see Figure S1 in the Supplement 1). Most especially, the $CsPbBr_3$ nanocrystals display the very low saturation intensity and excellent photobleaching resistance to the strong STED laser. When $CsPbBr_3$ QDs are excited from its ground S_0 to its excited state S_1, the excitons relax to the lowest vibrational sublevel of the S_1 state through efficient phonon coupling. In the presence of the STED light, the fluorescence decay ($k_f \sim 1/\tau_f$) competes with the stimulated emission process. If the STED intensity I_{STED} is much larger than the fluorescence intensity I_f, stimulated emission dominates over spontaneous emission and the fluorescence emission is effectively prevented by the STED beam. To make use of this switch-off process for improving the spatial resolution, the STED light is usually applied with the doughnut-shaped intensity distribution. Consequently, large I_{STED} intensities provide high spatial resolution.

3. Results and discussion

In order to investigate fluorescent properties of single particle in the high-density QDs regions, STED microscopy was performed to resolve QDs spaced closer beyond the optical diffraction limit. Figure 2 compares confocal and STED images of quantum dots in the high-density QDs regions. Unlike the confocal images (Fig. 2(a)), the STED images (Fig. 2(b)) clearly resolve closer QDs separated by <80 nm. Taking into account the similar brightness and full width at half maxima (FWHM) of images in the STED nanoscopy system, each individual QDs in the scan regions is resolved. Figure 2(c) shows the red linecuts through a subregion containing closely spaced QDs. Compared to the confocal images containing ensemble fluorescence images, the STED images reveal two fluorescence centers separated by 76 ± 2 nm (see Figure S4 in the Supplement 1).

In order to further investigate the influence of depletion power intensity on spatial resolution, the lateral resolutions of STED imaging were measured under the different STED depletion powers. As shown in Fig. 2(d), the measured spots size shrank rapidly with increased STED laser power and gradually saturated with further increases in STED laser power. The data in Fig. 2(d) is fitted by the following equation: $\Delta x \approx \lambda / \left(2N.A.\sqrt{1 + I_{STED}/I_{Sat}}\right)$, where λ is the wavelength of the fluorescent light, *N.A.* is the numerical aperture of the objective, I_{STED} is the depletion STED laser intensity, and I_{sat} is the saturation intensity of the fluorescent emitter. According to this equation, the lateral spatial resolution of STED nanoscopy is determined mainly by the intensity of the STED beam and the saturation intensity of the fluorescent emitter. The lateral resolution was close to 76 nm with the 2.5 mW STED depletion laser powers. The resolution can be increased mainly by increasing the intensity of the STED beam or by decreasing the saturation intensity of the fluorescent emitter.

On the basis of above confocal microscopy and STED nanoscopy, we used STED nanoscopy to resolve closer quantum dots beyond the optical diffraction limit. The second-order photon

Optics EXPRESS

correlation functions $g^2(\tau)$ were measured from single isolated QDs using the Hanbury Brown-Twiss detection setup. With pulsed excitation, a peak at zero delay time of the correlation function $g^2(0)$ of the recorded fluorescent signal is absent only for a single emitter. As a result, a notable peak at $g^2(0)$ from a single isolated QDs could not be detected in the STED images(Fig. 3(b)). However, in the confocal system for densely QDs sample, it only provides average information for QDs ensemble in a diffraction-limited volume(Fig. 3(a)). the PL intensity time traces of the high-density perovskite QDs regions are shown in confocal fluorescence image (Fig. 3(c)) and STED fluorescence images (Fig. 3(d)), respectively. Compared with STED fluorescence images, the PL intermittency is not apparent and fluorescence ON event is higher for confocal fluorescence image measurements due to aggregation of multiple quantum dots in the diffraction limit (see Fig. S2 in the Supplement 1). The fluorescence occurrence of ON and OFF periods in QDs has been usually attributed to the presence of an additional charge, which results in fluorescence quenching by nonradiative Auger recombination. This Auger process not only quenches fluorescence but it also suppresses multiexcitonic emission. Therefore, even at high-power excitation close to saturation, only single exciton emission occurs as shown in Fig. 3(b).

Compared to all-inorganic $CsPbBr_3$ QDs, the in-situ microscopy observations of nanostructural features in perovskite thin films are crucial to improving the material quality and the corresponding performance. Despite tremendous improvements to power conversion efficiencies, the role of

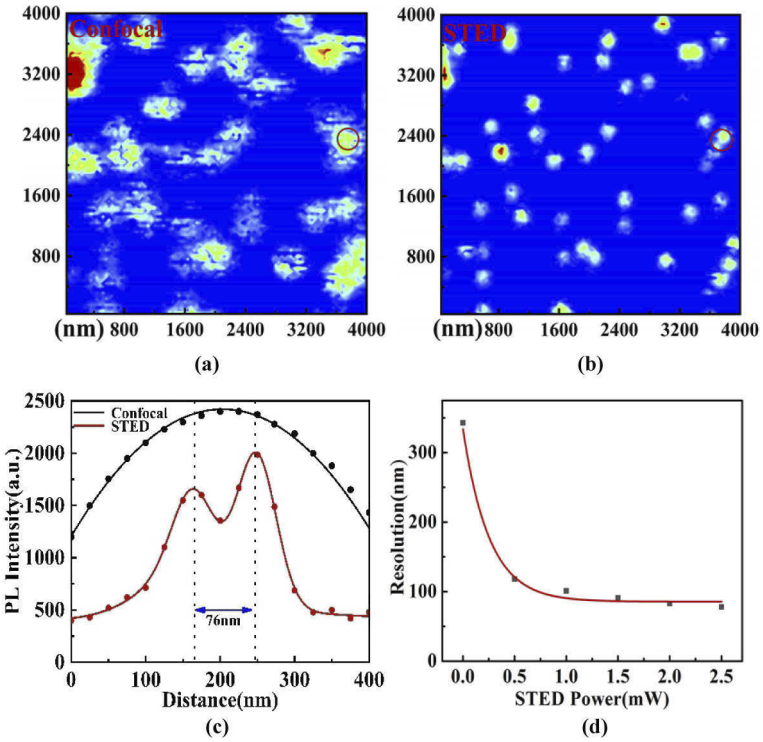

Fig. 2. (a) Confocal imaging of $CsPbBr_3$ QDs excited by a 405 nm pulse laser (0.5μW); (b) STED images excited by the 405 nm laser (0.5μW) and the 568 nm STED continuous laser (2.5 mW); (c) Linecuts of the confocal (black) and STED (red) images across the dashed lines annotated in (a) and (b), respectively. The red solid line is a fit to two Gaussian functions, revealing a closer QDs separation of 76 ± 2 nm; (d) normalized fluorescence intensity profiles along the lines across the QDs irradiated by the STED laser with 0.01, 0.5, 1.5, and 2.0 mW, 2.5 mW.

Optics EXPRESS

boundaries or buried interfaces of local nanostructures in perovskite thin films is currently under debate. We show that restriction of the measurements to local nanostructures permits understanding of the carrier dynamics process not possible for study of ensembles. Therefore, direct in-situ carrier dynamics measurements of perovskite thin films at the nanometer scale are vital.

To investigate the in-situ optical properties and carrier dynamics of nanostructures in the perovskite films, we used the STED fluorescence microscopy to probe the local PL spectrum and PL decay properties of perovskite thin films at the nanometer scale. Figure 4 shows a correlated SEM micrograph(Fig. 4(a)), confocal PL image(Fig. 4(b)), and STED PL microscopy image (Fig. 4(c)) of the perovskite film on a glass substrate(see Fig. S3 in the Supplement 1). Figure 4(b) and 4(c) compares the corresponding confocal and STED images from the same high-density perovskite films regions. Taking into account the brightness and full width at half maxima intensity of STED images, it obviously indicate that each individual fluorescence center of nanostructure in the scan region is resolved. Figure 4(d) shows linecuts through a subregion containing closely spaced fluorescent centers of nanostructures (red lines in Fig. 4(b,c)). Compared to the confocal images containing ensemble fluorescence images, the STED images reveal two fluorescence centers separated by 94 ± 2 nm (see Figure S5 in the Supplement 1).

Fluorescence blinking has been extensively investigated in semiconductor nanostructures, providing unique insight into their photo-excited carrier dynamics process. Here, we investigate the fluorescence intensity time traces from the same perovskite thin film marked regions (red linecuts) in confocal fluorescence image (Fig. 5(a)) and STED fluorescence images (Fig. 5(b)), respectively. We have found that fluorescence blinking is present in the confocal fluorescence image whereby nanostructures are in close contact with one another. Therefore, it facilitates

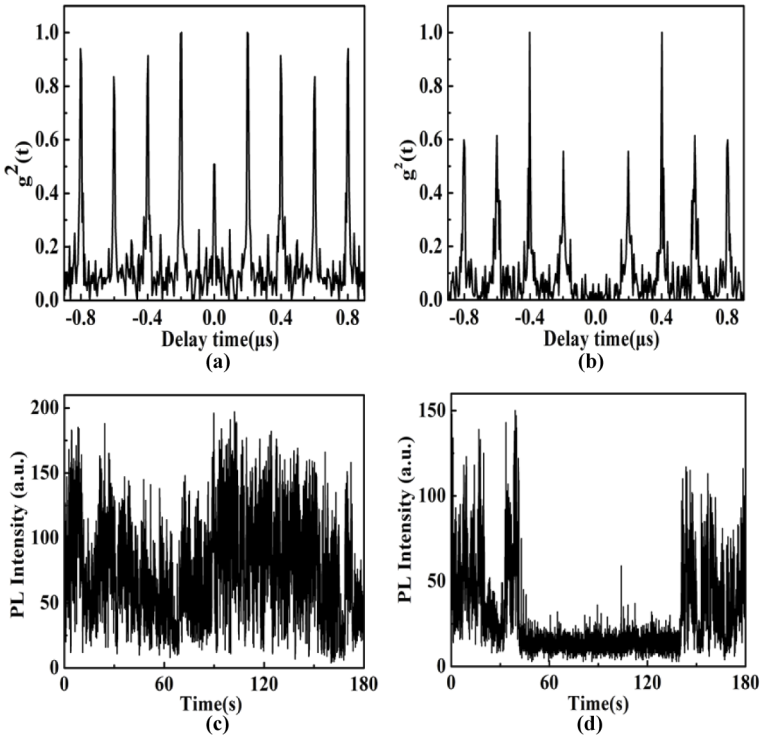

Fig. 3. Correlation function $g^2(\tau)$ of (a) confocal and (b) STED detection; fluorescence intensity time traces in Confocal fluorescence image (c) and STED fluorescence images (d).

Optics EXPRESS

exciton nonradiative recombination at the interfaces or at the boundary of the nanostructures. This leads to enhanced fluorescence intermittency contributing to nonradiative recombination. On the other hand, fluorescence blinking is not present in the STED fluorescence images. Blinking appeared to be largely suppressed by high power STED laser excitation due to surface passivation. Photon antibunching measurements were also carried out on the nanostructures of perovskite thin films from confocal system (Fig. 5(c)) and STED system(Fig. 5(d)). The second-order correlation functions $g^2(t)$ demonstrate that neither the isolated nanostructures in the STED images nor the thin film in the confocal images shows single photon emissions.

In order to further study the in-situ dynamics process of excited carriers in nanostructured regions, the corresponding local PL spectrum and PL lifetime of confocal fluorescence image and STED fluorescence images are investigated, respectively. The local spectra of bright (red) and dim(black) region in the confocal fluorescence images are shown in Fig. 6(a), respectively. the PL spectra at the dim region is both red-shifted (~2 nm) and slightly broader by contrast with the bright region. These trends attribute to the presence of defect states or shallow trapping levels in the boundary regions. Figure 6(c) shows the corresponding PL decay for bright (red) and dim(black) region in the confocal fluorescence images, respectively. The PL decay of bright regions can appear single-exponential with an average lifetime of 21.3 ns. The PL decay of dim regions fitted by biexponential functions $A_1 \exp(-t/\tau_1) + A_2 \exp(-t/\tau_2)$, demonstrating the nonradiative trapped lifetime ~2.4 ns and radiative recombination lifetime ~19.7 ns, respectively. It should be emphasized that the PL intensity time traces at the dim regions are evidently different from those at the bright regions due to different decay mechanisms.

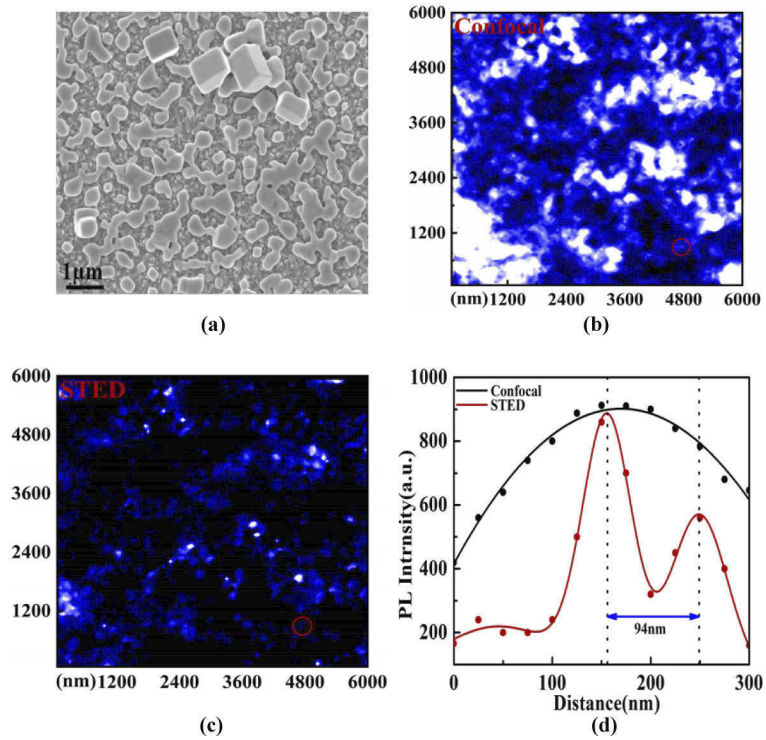

Fig. 4. (a) SEM image; (b) Confocal fluorescence image and (c) STED fluorescence images from the same perovskite film region. (d) Linecuts of the confocal (black) and STED (red) images across the dashed lines annotated in (b) and (c), respectively. The red solid line is a fit to two Gaussian functions, revealing a fluorescence center separation of 94 ± 2 nm.

Optics EXPRESS

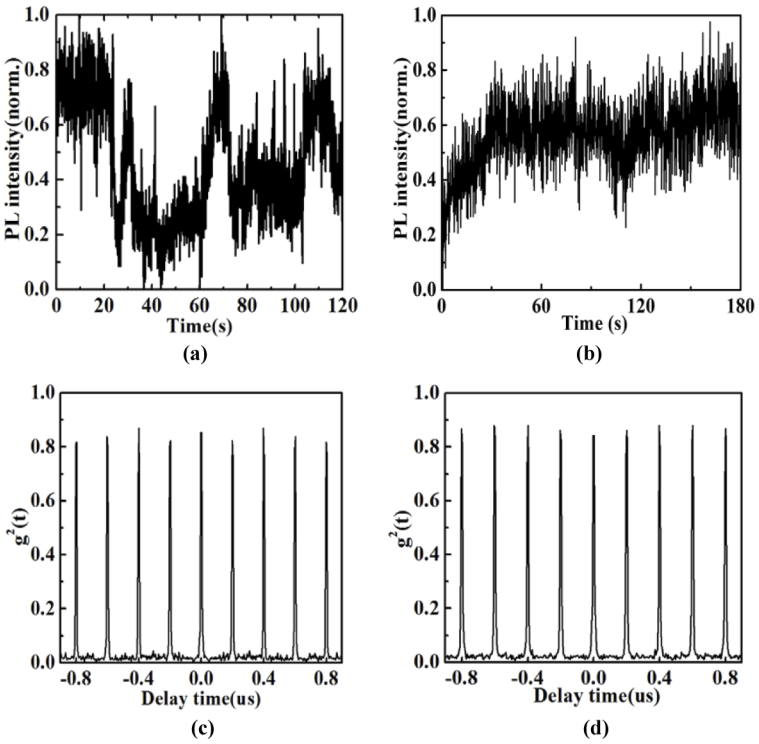

Fig. 5. (a) Fluorescence intensity time traces and (c) photon antibunching measurements in the confocal system; (b) fluorescence intensity time traces and (d) photon antibunching measurements in the STED system.

Figure 6(b) shows local steady-state PL spectra of bright (red) and dim(black) region for the indicated individual nanostructure in the STED fluorescence images. In contrast to PL intensity of the same dim regions in the confocal system as shown in Fig. 6(a), the relative PL intensity is greatly increased by approximative 5 times in the STED system. The PL emission spectrum was blue-shifted (by~3 nm) and narrowed slightly after STED laser beam excitation, which could be caused by the reduction in shallow trapped states density. Among the factors that affect perovskite stability, light is particularly important for surface passivation. The interaction between light and perovskite is found to be dependent on relevant factors. For example, the presence of oxygen or a rise in temperature can passivate under-coordinated Pb^{2+} vacancies in perovskite films and eliminated the shallower trap states due to Pb ions defects. In Fig. 6(d), we show the corresponding local PL decays of the indicated dim(13.5 ns) and bright regions(20.5 ns), respectively. These results indicates that STED laser indeed passivate defect states of nanostructure boundary regions and inhibit the nonradiative recombination in the perovskite thin films.

Optics EXPRESS

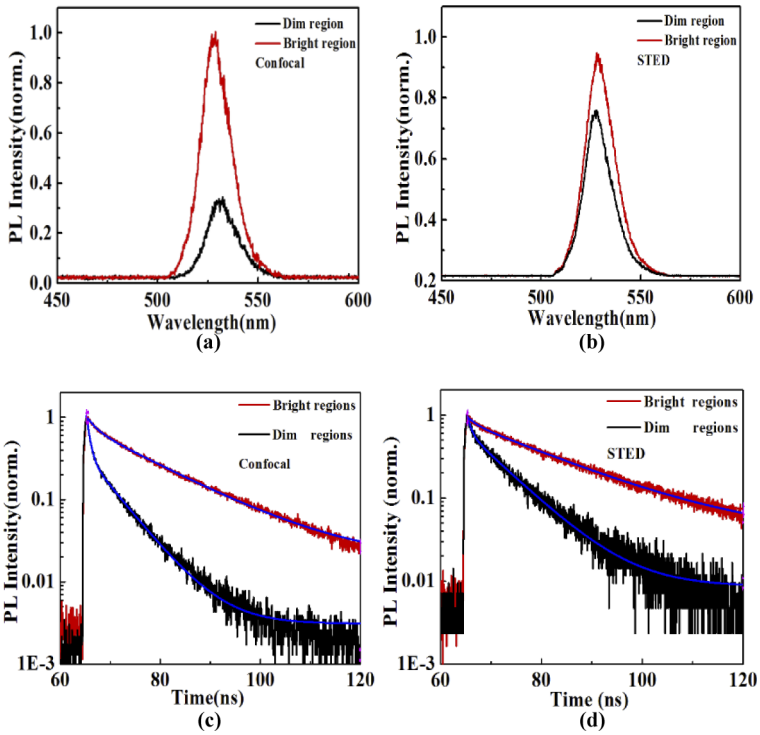

Fig. 6. local PL spectra of confocal image (a) and STED image (b) with corresponding PL spectra of bright (red line) and dim (black line) regions, respectively; Time-resolved PL decay curves of confocal image (c) and STED image (d) with corresponding bright (red line) and dim (black line) regions, respectively.

4. Conclusions

In conclusion, we used STED nanoscopy to resolve single QDs and nanostructures embedded inside high-dense perovskite thin films beyond the optical diffraction limit and investigated the second-order correlation function $g^2(t)$ and PL blinking of the nanostructures at the single particle level. These results revealed the different physical origin of PL blinking and photon antibunching phenomena for QDs and nanostructures of perovskite thin films, respectively. Overall, these results highlighted the importance of fluorescence behaviors and carrier dynamics correlated to the nanostructures of perovskite thin films at the nanometer scale. The unique insights gained from such studies are essential for guiding nanostructured tailoring of perovskite films for improving optical performance in future optoelectronic devices application.

Funding. Taishan Scholar Project of Shandong Province (ts201511055, tsqn201812098); Natural Science Foundation of Shandong Province (ZR2019MA066, ZR2019MF057); National Natural Science Foundation of China (61905106); High School Science and Technology Funding Planning Project of Shandong Province of China (J18KA222).

Disclosures. The authors declare no conflicts of interest.

Data availability. No data were generated or analyzed in the presented research.

Supplemental document. See Supplement 1 for supporting content.

References

1. A. Kojima, K. Teshima, Y. Shirai, and T. Miyasaka, "Organometal Halide Perovskites as Visible-Light Sensitizers for Photovoltaic Cells," J. Am. Chem. Soc. **131**(17), 6050–6051 (2009).
2. M. M. Lee, J. Teuscher, T. Miyasaka, T. N. Murakami, and H. J. Snaith, "Efficient Hybrid Solar Cells Based on Meso-Superstructured Organometal Halide Perovskites," Science **338**(6107), 643–647 (2012).

Optics EXPRESS

3. W. S. Yang, B. W. Park, E. H. Jung, N. J. Jeon, Y. C. Kim, D. U. Lee, S. S. Shin, J. Seo, E. K. Kim, J. H. Noh, and S. I. Seok, "Iodide Management in Formamidinium-Lead-Halide-Based Perovskite Layers for Efficient Solar Cells," Science **356**(6345), 1376–1379 (2017).
4. M. Saliba, T. Matsui, J. Y. Seo, K. Domanski, J. P. Correa-Baena, M. K. Nazeeruddin, S. M. Zakeeruddin, W. Tress, A. Abate, A. Hagfeldt, and M. Gratzel, "Cesium-containing Triple Cation Perovskite Solar Cells: Improved Stability, Reproducibility and High Efficiency," Energy Environ. Sci. **9**(6), 1989–1997 (2016).
5. T. M. Brenner, D. A. Egger, L. Kronik, G. Hodes, and D. Cahen, "Hybrid Organic-Inorganic Perovskites: Low-Cost Semiconductors with Intriguing Charge-Transport Properties," Nat. Rev. Mater. **1**(1), 15007 (2016).
6. Y. H. Kim, C. Wof, Y. T. Kim, H. Cho, W. Kwon, S. Do, A. Sadhanala, C. G. Park, S. W. Rhee, S. H. Im, R. H. Friend, and T. W. Leet, "Highly Efficient Light-Emitting Diodes of Colloidal Metal-Halide Perovskite Nanocrystals beyond Quantum Size," ACS Nano **11**(7), 6586–6593 (2017).
7. F. Fang, W. Chen, Y. Li, H. C. Liu, M. Mei, R. Zhang, J. J. Hao, M. Mikita, W. Q. Cao, R. K. Pan, K. Wang, and X. W. Sun, "Employing Polar Solvent Controlled Ionization in Precursors for Synthesis of High-Quality Inorganic Perovskite Nanocrystals at Room Temperature," Adv. Funct. Mater. **28**(10), 1706000 (2018).
8. S. Yakunin, L. Protesescu, F. Krieg, M. I. Bodnarchuk, G. Nedelcu, M. Humer, G. De Luca, M. Fiebig, W. Heiss, and M. V. Kovalenko, "Low-threshold Amplified Spontaneous Emission and Lasing from Colloidal Nanocrystals of Caesium Lead Halide Perovskites," Nat. Commun. **6**(1), 8056 (2015).
9. Y. Wang, X. M. Li, J. Z. Song, L. Xiao, H. B. Zeng, and H. D. Sun, "All-Inorganic Colloidal Perovskite Quantum Dots: A New Class of Lasing Materials with Favorable Characteristics," Adv. Mater. **27**(44), 7101–7108 (2015).
10. Y. Wang, X. M. Li, X. Zhao, L. Xiao, H. B. Zeng, and H. D. Sun, "Nonlinear Absorption and Low-Threshold Multiphoton Pumped Stimulated Emission from All-Inorganic Perovskite Nanocrystals," Nano Lett. **16**(1), 448–453 (2016).
11. J. S. Manser, J. A. Christians, and P. V. Kamat, "Intriguing Optoelectronic Properties of Metal Halide Perovskites," Chem. Rev. **116**(21), 12956–13008 (2016).
12. J. Liang, C. X. Wang, Y. R. Wang, Z. R. Xu, Z. P. Lu, Y. Ma, H. F. Zhu, Y. Hu, C. C. Xiao, X. Yi, G. Y. Zhu, H. L. Lv, L. B. Ma, T. Chen, Z. X. Tie, Z. Jin, and J. Liu, "All-Inorganic Perovskite Solar Cells," J. Am. Chem. Soc. **138**(49), 15829–15832 (2016).
13. Q. S. Ma, S. J. Huang, X. M. Wen, M. A. Green, and A. W. Y. Ho-Baillie, "Hole Transport Layer Free Inorganic $CsPbIBr_2$ Perovskite Solar Cell by Dual Source Thermal Evaporation," Adv. Energy Mater. **6**(7), 1502202 (2016).
14. E. M. Hutter, R. J. Sutton, S. Chandrashekar, M. Abdi-Jalebi, S. D. Stranks, H. J. Snaith, and T. J. Sayenije, "Vapour-Deposited Cesium Lead Iodide Perovskites: Microsecond Charge Carrier Lifetimes and Enhanced Photovoltaic Performance," ACS Energy Lett. **2**(8), 1901–1908 (2017).
15. C. Liu, W. Z. Li, J. H. Chen, J. D. Fan, Y. H. Mai, and R. E. I. Schropp, "Ultra-thin MoO_x as Cathode Buffer Layer For the Improvement of All-inorganic $CsPbIBr_2$ Perovskite Solar Cells," Nano Energy **41**, 75–83 (2017).
16. T. Y. Zhang, M. I. Dar, G. Li, F. Xu, N. J. Guo, M. Gratzel, and Y. X. Zhao, "Bication Lead Iodide 2D Perovskite Component to Stabilize Inorganic α-$CsPbI_3$ Perovskite Phase for High-efficiency Solar Cells," Sci. Adv. **3**(9), 6 (2017).
17. J. Burschka, N. Pellet, S. J. Moon, R. Humphry-Baker, P. Gao, M. K. Nazeeruddin, and M. Gratzel, "Sequential Deposition as a Route to High-Performance Perovskite-Sensitized Solar Cells," Nature **499**(7458), 316–319 (2013).
18. G. E. Eperon, V. M. Burlakov, P. Docampo, A. Goriely, and H. J. Snaith, "Morphological Control for High Performance, Solution-Processed Planar Heterojunction Perovskite Solar Cells," Adv. Funct. Mater. **24**(1), 151–157 (2014).
19. H. P. Zhou, Q. Chen, G. Li, S. Luo, T. B. Song, H. S. Duan, Z. R. Hong, J. B. You, Y. S. Liu, and Y. Yang, "Interface Engineering of Highly Efficient Perovskite Solar Cells," Science **345**(6196), 542–546 (2014).
20. N. K. Noel, A. Abate, S. D. Stranks, E. S. Parrott, V. M. Burlakov, A. Goriely, and H. J. Snaith, "Enhanced Photoluminescence and Solar Cell Performance via Lewis Base Passivation of Organic Inorganic Lead Halide Perovskites," ACS Nano **8**(10), 9815–9821 (2014).
21. A. Abate, M. Saliba, D. J. Hollman, S. D. Stranks, K. Wojciechowski, R. Avolio, G. Grancini, A. Petrozza, and H. J. Snaith, "Supramolecular Halogen Bond Passivation of Organic-Inorganic Halide Perovskite Solar Cells," Nano Lett. **14**(6), 3247–3254 (2014).
22. D. W. deQuilettes, S. M. Vorpahl, S. D. Stranks, H. Nagaoka, G. E. Eperon, M. E. Ziffer, H. J. Snaith, and D. S. Ginger, "Impact of Microstructure on Local Carrier Lifetime in Perovskite Solar Cells," Science **348**(6235), 683–686 (2015).
23. Z. D. Chu, M. J. Yang, P. Schulz, D. Wu, X. Ma, E. Seifert, L. Y. Sun, X. Q. Li, K. Zhu, and K. J. Lai, "Impact of Grain Boundaries on Efficiency and Stability of Organic-Inorganic Trihalide Perovskites," Nat. Commun. **8**(1), 8 (2017).
24. T. S. Sherkar, C. Momblona, L. Gil-Escrig, J. Avila, M. Sessolo, H. J. Bolink, and L. J. A. Koster, "Recombination in Perovskite Solar Cells: Significance of Grain Boundaries, Interface Traps, and Defect Ions," ACS Energy Lett. **2**(5), 1214–1222 (2017).
25. H. M. Wang, Z. Q. Q. Feng, S. J. Del Signore, A. A. Rodal, and B. Xu, "Active Probes for Imaging Membrane Dynamics of Live Cells with High Spatial and Temporal Resolution over Extended Time Scales and Areas," J. Am. Chem. Soc. **140**(10), 3505–3509 (2018).

Optics EXPRESS

26. H. Sai, G. C. Lau, A. J. Dannenhoffer, S. M. Chin, L. Dordevic, and S. I. Stupp, "Imaging Supramolecular Morphogenesis with Confocal Laser Scanning Microscopy at Elevated Temperatures," Nano Lett. **20**(6), 4234–4241 (2020).
27. A. Sarkar, S. Dhiman, A. Chalishazar, and S. J. George, "Visualization of Stereoselective Supramolecular Polymers by Chirality-Controlled Energy Transfer," Angew. Chem. Int. Ed. **56**(44), 13767–13771 (2017).
28. Y. R. Fang Z, L. Zhang, and M. T. Sun, "High vacuum tip-enhanced Raman spectroscope based on a scanning tunneling microscope," Rev. Sci. Instrum. **87**(3), 033104 (2016).
29. L. R. Parent, E. Bakalis, A. Ramirez-Hernandez, J. K. Kammeyer, C. Park, J. J. de Pablo, F. Zerbetto, J. P. Patterson, and N. C. Gianneschi, "Directly Observing Micelle Fusion and Growth in Solution by Liquid-Cell Transmission Electron Microscopy," J. Am. Chem. Soc. **139**(47), 17140–17151 (2017).
30. M. T. Proetto, A. M. Rush, M. P. Chien, P. A. Baeza, J. P. Patterson, M. P. Thompson, N. H. Olson, C. E. Moore, A. L. Rheingold, C. Andolina, J. Millstone, S. B. Howell, N. D. Browning, J. E. Evans, and N. C. Gianneschi, "Dynamics of Soft Nanomaterials Captured by Transmission Electron Microscopy in Liquid Water," J. Am. Chem. Soc. **136**(4), 1162–1165 (2014).
31. D. J. Muller and Y. F. Dufrene, "Atomic Force Microscopy as a Multifunctional Molecular Toolbox in Nanobiotechnology," Nat. Nanotechnol. **3**(5), 261–269 (2008).
32. S. W. Hell, "Far-field Optical Nanoscopy," Science **316**(5828), 1153–1158 (2007).
33. S. W. Hell and J. Wichmann, "Breaking the Diffraction Resolution Limit by Stimulated Emission: Stimulated-Emission-Depletion Fluorescence Microscopy," Opt. Lett. **19**(11), 780–782 (1994).
34. H. Blom and J. Widengren, "Stimulated Emission Depletion Microscopy," Chem. Rev. **117**(11), 7377–7427 (2017).
35. X. H. Tian, C. De Pace, L. Ruiz-Perez, B. Chen, R. N. Su, M. Z. Zhang, R. L. Zhang, Q. Zhang, Q. Wang, H. P. Zhou, J. Y. Wu, Z. P. Zhang, Y. P. Tian, and G. Battaglia, "A Cyclometalated Iridium (III) Complex as a Microtubule Probe for Correlative Super-Resolution Fluorescence and Electron Microscopy," Adv. Mater. **32**(39), 2003901 (2020).
36. S. Onogi, H. Shigemitsu, T. Yoshii, T. Tanida, M. Ikeda, R. Kubota, and I. Hamachi, "In Situ Real-time Imaging of Self-sorted Supramolecular Nanofibres," Nat. Chem. **8**(8), 743–752 (2016).
37. L. Protesescu, S. Yakunin, M. I. Bodnarchuk, F. Krieg, R. Caputo, C. H. Hendon, R. X. Yang, A. Walsh, and M. V. Kovalenko, "Nanocrystals of Cesium Lead Halide Perovskites ($CsPbX_3$, X = Cl, Br, and I): Novel Optoelectronic Materials Showing Bright Emission with Wide Color Gamut," Nano Lett. **15**(6), 3692–3696 (2015).
38. S. Sun, D. Yuan, Y. Xu, A. Wang, and Z. Deng, "Ligand-Mediated Synthesis of Shape-Controlled Cesium Lead Halide Perovskite Nanocrystals via Reprecipitation Process at Room Temperature," ACS Nano **10**(3), 3648–3657 (2016).
39. F. Liu, Y. Zhang, C. Ding, S. Kobayashi, T. Izuishi, N. Nakazawa, T. Toyoda, T. Ohta, S. Hayase, T. Minemoto, K. Yoshino, S. Dai, and Q. Shen, "Highly Luminescent Phase-Stable $CsPbI_3$ Perovskite Quantum Dots Achieving Near 100% Absolute Photoluminescence Quantum Yield," ACS Nano **11**(10), 10373–10383 (2017).